Morphology and size of soot from gas flares as a function of fuel and water addition

Trivanovic, Una; Sipkens, Timothy A.; Kazemimanesh, Mohsen; Baldelli, Alberto; Jefferson, A. Melina; Conrad, Bradley M.; Johnson, Matthew R.; Corbin, Joel C.; Olfert, Jason S.; Rogak, Steven N.

Publisher's version / Version de l'éditeur:
https://doi.org/10.1016/j.fuel.2020.118478
Fuel, 279, pp. 1-10, 2020-07-10

Morphology and size of soot from turbulent diffusion flames as a function of fuel and water addition

Una Trivanovic*[,a], Timothy A. Sipkens[a], Mohsen Kazemimanesh[b], Alberto Baldelli[a], A. Melina Jefferson[c], Bradley M. Conrad[d], Matthew R. Johnson[d], Joel C. Corbin[e], Jason S. Olfert[b], Steven N. Rogak[a]

[a] *Department of Mechanical Engineering, University of British Columbia, Vancouver, BC Canada*
[b] *Department of Mechanical Engineering, University of Alberta, Edmonton, AB, Canada*
[c] *Natural Resources Canada, Ottawa, ON, Canada*
[d] *Department of Mechanical and Aerospace Engineering, Carleton University, Ottawa, ON, Canada*
[e] *Metrology Research Centre, National Research Council Canada, 1200 Montreal Rd, Ottawa, ON K1A 0R6, Canada*

Abstract

A large-scale, laboratory turbulent diffusion flame was used to study the effects of fuel composition on soot size and morphology. The burner and fuels are typical of those used in the oil and gas industry for gas flaring, a practice commonly used to dispose of excess gas. Fuels were characterized by their carbon-to-hydrogen ratio (from 0.264 to 0.369) and their volumetric higher heating value (HHVv) (from 35.8 to 75.2 MJ/m^3). Transmission electron microscopy (TEM) was used to assess primary particle and aggregate size, showing that the scaling of primary particle size to aggregate size was roughly the same for all of the considered fuels (d_p = 16.3(d_a [nm]/100)$^{0.35}$). A scanning mobility particle sizer (SMPS) was also used (i) to measure mobility diameter distributions and (ii) in tandem with a centrifugal particle mass analyzer (CMPA) to determine the effective density of the particles. A new inversion approach was applied to determine the two-dimensional mass-mobility and effective density-mobility distributions. The new approach was shown to improve consistency of inferred morphological parameters, though with a shift relative to median-based analysis of the tandem data. Raman spectroscopy was used to quantify the degree of graphitization in the soot nanostructure. The HHVv of the fuel had a strong effect on the size of the soot with higher HHVv fuels producing larger aggregates. Larger aggregates also tended to have larger primary particles and higher Raman D/G ratios suggesting larger graphitic domains.

1. Introduction

Gas flaring is ubiquitous in the oil and gas industry where excess gas is burned off, both routinely when it is not economical to capture a gas, and in emergencies. In 2012, an estimated 143x10^9 m^3 of gas was flared globally [1] while in 2018 this number has risen to 145x10^9 m^3 [2]. As with many combustion processes, gas flaring produces soot, formed during the incomplete combustion of hydrocarbons. Soot has established negative impacts on human health [3, 4, 5] and has a positive radiative forcing effect making it an important contributor to climate change [6]. The severity of these effects depends on the morphology of the particles. For example, morphology is related to the optical properties of a particle while particle size determines where in the lungs the particles are deposited [7]. Aerosols are leading contributors of

* Corresponding author
Email address: [unat@mail.ubc.ca] (U. Trivanovic)

uncertainties in current climate models [8, 9] and thus accurate quantification of soot morphology and release rates could improve climate models and estimates of the remaining carbon budget. Soot is particularly important in the Arctic where the effects of soot are enhanced due to low lying clouds and deposition on snow and ice [10, 11]. Nearly half of soot emissions in the Arctic are estimated to come from gas flaring due to high volumes of flaring in Russia, the North Sea and the Norwegian Sea [12]. Despite this, the environmental effects of flaring have been poorly characterized and often over-looked in the past [13].

Gas flares are large-scale buoyant turbulent flames, which often limits accessibility and has restricted the number of detailed studies of soot emissions. A number of studies have estimated soot yields from flares using downstream aircraft measurements [14, 15, 16, 17], a mobile laboratory [18] or long-range optical measurements such as sky-LOSA [19, 20, 21]. Of these studies only two reported mass median diameter [16, 17] and one reported the mass distribution [17]. Instead, researchers have begun studying lab-based gas flares with varying amounts of morphological information [22, 23, 24].

The current study investigates the effect of industry-representative fuels on the size and morphology of soot generated from a large, buoyant turbulent diffusion flame located at the Carleton University Flare Facility. Emissions from the flare are sent through a dilution tunnel and analyzed with a suite of online and offline instrumentation downstream. Fourteen different fuel compositions, representative of the range observed in the global oil and gas flaring industry, are studied. The effect of entrained water, which may occur during hydraulic fracturing, is also briefly considered. The fuel range used here greatly expands upon the range used by Kazemimanesh et al. [23] at the same facility. The primary particle size, aggregate size, mobility diameter, effective density and degree of graphitization are reported as a function of the fuel's volumetric higher heating value (HHVv). Two-dimensional forms of analysis are used to provide detailed information about the range of morphologies produced that may not be evident in simpler, one-dimensional analyses. Due to soot's highly heterogenous structures, this type of analysis gives a much better description of the true aerosol population.

2. Methods and materials

Soot particles were generated from a buoyant turbulent diffusion flame at the Carleton University Flare Facility, described in detail by Kazemimanesh et al. [23]. A schematic of the overall setup is provided in Figure 1. The burner was 2-inches in diameter and all tests were run at a flowrate of 156 SLPM (standard litres per minute, 0°C, 100 kPa) of fuel. Particles were collected by a ventilation hood placed above the flare, naturally providing dilution in the range of ~ 16:1 to ~ 64:1. Instruments pulled samples from an insulated tunnel connected to the ventilation hood with pumps and flow control built into the equipment.

Fuels were composed of mixtures of methane, ethane, propane, *n*-butane, nitrogen, carbon dioxide, isopentane, *n*-hexane, and *n*-heptane and were chosen to represent the range of flaring fuels in the global oil and gas industry. The fuel codes, fuel composition, carbon-to-hydrogen ratio (C:H), geographic region, and volumetric higher heating values (HHVv) are listed in table S1 of the supplemental material. The L9, M9, and H9 fuels span the typical compositions of fuels commonly found in Alberta, Canada; BK-BR and BK-WO represent fuels from the Bakken region in North Dakota, USA; EC-AC, EC-AS and EC-A27 are representative of fuels from Ecuador; RU-KM1, RU-KM2 and RU-FI are representative of fuels from

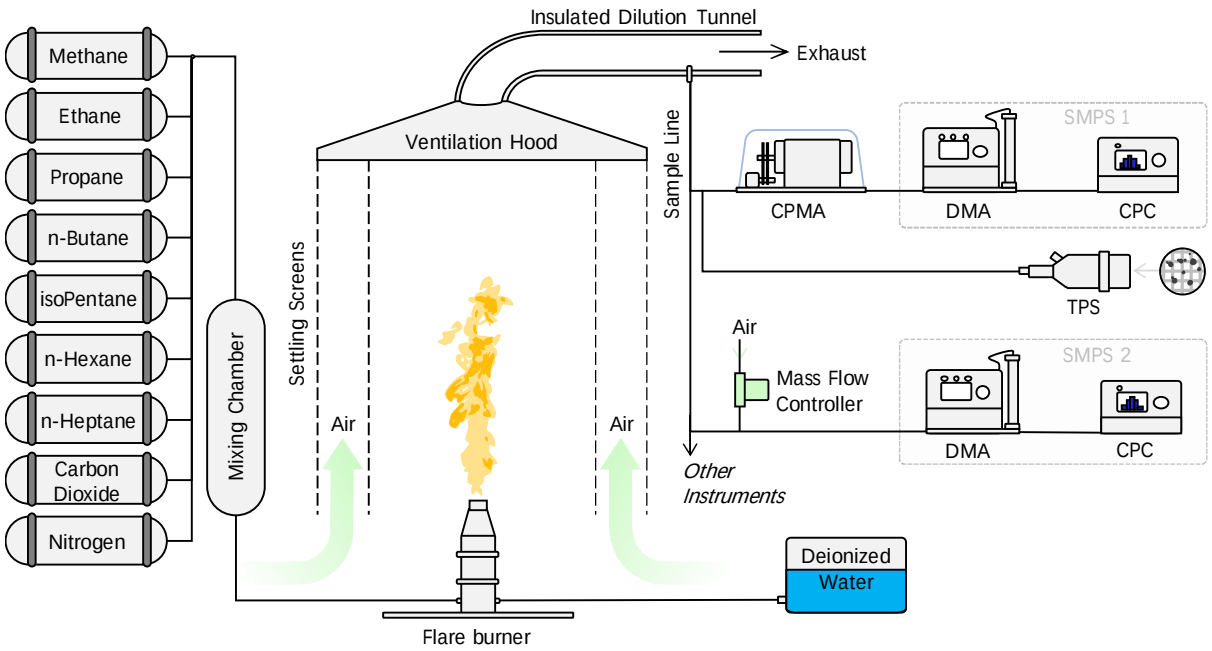

Figure 1. A schematic of the experimental setup at the Carleton Flare Facility, including the input gases, atomizer, and different instrument arrangements.

Russia; and NS-M9 is an average fuel composition of 20 platforms in the North Sea. In addition, results in this study are compared to data from Kazemimanesh et al. [23], which are labeled L6, M6 and H6, and to a lesser extent to the results of Popovicheva et al. [24]. Typical fuel compositions of gas flares in western Canada were determined by Johnson and Coderre [25]. In this study, the fuels are primarily characterized by their HHVv and span a large range, with the highest HHVv (75.17 MJ/m^3) being more than double the lowest HHVv (35.8 MJ/m^3). HHVv in this case is a theoretical value, calculated based on the target fuel composition and indicates the heat of combustion [24].

An ultrasonic atomizer (Sono-Tek Inc., Model NZL120CO) was used to introduce a narrow conical pattern of deionized water droplets into the flame. The atomizer was concentric with the burner outlet and was adjusted at ~75 mm below the exit plane of the burner outlet. The ultrasonic atomizer, powered with a frequency generator at 120 kHz, atomized the water at a flow rate of 13 mL/min. Based on the atomizer specifications, the median diameter of the droplets was 19 µm. The liquid was delivered to the atomizer via a precision micro-gear pump (Ismatec/Cole-Parmer, Model ISM901B), which had a bias uncertainty of 3%. The pump was calibrated by measuring the total mass of liquid pumped over a specific time to determine the mass flow rate, which was converted to the volumetric flow rate using the liquid density at room temperature.

2.1 SMPS and CPMA characterization

Particle mobility distributions were characterized using a scanning mobility particle sizer (SMPS), which consists of a differential mobility analyzer (DMA; TSI Inc., Model 3081) and a condensation particle counter (CPC; TSI Inc., Model 3776). The aerosol and sheath air flow rates were 0.3 L/min and 3.0 L/min, respectively. The default inversion approach provided by the TSI's Aerosol Instrument Manager (AIM) software was used to retrieve the mobility diameter distribution of the particles. The mobility diameter distributions were corrected for multiple charging and diffusion losses using TSI's built-in inversion. The sample from the duct was further diluted by adding a known flow rate of particle-free dry air to the sample using a mass flow controller upstream of the SPMS. The dilution factor varied from 1 to ~13.5, depending on the particle concentration in each test. The dilution factor was measured by comparing the CO_2 mole

fraction of the undiluted and diluted samples for each test case using a non-dispersive infrared CO_2 analyzer (LiCor Inc., Model LI-850).

A second SMPS was paired with a centrifugal particle mass analyzer (CPMA; Cambustion Ltd.) on a separate line to simultaneously measure particle mass and mobility diameter. Measurements take the form of a series of SMPS scans, each at a single setpoint of the CPMA. Morphological parameters were derived from these measurements using the mass-mobility relation, a correlation of the form

$$\bar{m}|d_\mathrm{m} = k d_\mathrm{m}^{D_\mathrm{m}} = m_{100}\left(\frac{d_\mathrm{m}}{100\ \mathrm{nm}}\right)^{D_\mathrm{m}}, \tag{1}$$

where $\bar{m}|d_\mathrm{m}$ is a measure of the average mass of particles having a given mobility diameter, d_m; k and D_m are the mass-mobility pre-factor and exponent and are fitting parameters; and m_{100} is the expected mass of a particle with d_m = 100 nm. It is also common to consider the effective density of the particles, defined for any particle as

$$\rho_\mathrm{eff} \equiv \frac{m}{\pi d_\mathrm{m}^3/6}. \tag{2}$$

Using $\bar{m}|d_\mathrm{m}$, one can define a correlation equivalent to Eq. (1) for some measure of the average effective density as

$$\bar{\rho}_\mathrm{eff}|d_\mathrm{m} = \frac{m_\mathrm{g}|d_\mathrm{m}}{\pi d_\mathrm{m}^3/6} = \frac{6}{\pi} k (d_\mathrm{m})^{D_\mathrm{m}-3} = \rho_{\mathrm{eff},100}\left(\frac{d_\mathrm{m}}{100\ \mathrm{nm}}\right)^{D_\mathrm{m}-3}, \tag{3}$$

where $\rho_{\mathrm{eff},100}$ is the effective density of a particle with d_m = 100 nm.

The tandem measurements were interpreted in two ways. First, in a *median-based approach*, the conditional mobility distribution was assumed to be lognormal. The morphological parameters, k and m_{100}, can then be determined by fitting Eq. (1) to data pairs formed by: (*i*) the median of a lognormal distribution fit to the mass-selected SMPS scans (i.e. to the conditional mobility distribution) and (*ii*) the setpoint mass (assuming a singly charged particle). In the present work, fitting was performed using a weighted least-squares analysis, where weights on each of the median mobility diameters was determined from uncertainties in the lognormal distribution fitting procedure. This resulted in lower weights in the cases of low signal, where uncertainties in the retrieved median mobility diameter are larger. The parameters can be equally derived from Eq. (3) using data pairs consisting of the median mobility and effective density, with

nearly identical results. This represents the more traditional analysis of the tandem measurements, as has been performed in some form previously (e.g. [23, 25]).

Second, additional information can be extracted from the measurements by using the tandem arrangement to determine the two-dimensional mass-mobility distribution. Originally introduced by Rawat et al. [25], this interpretation represents the measurements as

$$N_i = \int_0^\infty \int_0^\infty K(\mathbf{r}_i^*, m, d_\mathrm{m}) \cdot \frac{\partial^2 n}{\partial \log_{10} m \cdot \partial \log_{10} d_\mathrm{m}} \cdot \mathrm{d}\log_{10} d_\mathrm{m} \cdot \mathrm{d}\log_{10} m + \varepsilon_i \,. \tag{4}$$

where N_i is the number of particles measured at a given setpoint for the SMPS and CPMA; $K(\mathbf{r}_i^*, m, d_\mathrm{m})$ is the kernel, which describes the instrument transfer function at setpoint $\mathbf{r}_i^* = [m_i^*, d_{\mathrm{m},i}^*]$, where m^* is the mass setpoint for a singly charged particle and d_m^* is the mobility diameter setpoint; $\partial^2 n/\partial\log_{10} m \cdot \partial\log_{10} d_\mathrm{m}$ is the number-based two-dimensional mass-mobility distribution; and ε_i is the error in the i^{th} measurement. Retrieval of the mass-mobility distribution requires a different treatment of the data inversion, of which we refer the reader to previous works [26, 27, 28] and the supplemental material. The present work employed a Bayesian approach to inversion, using an exponential distance prior that correlates points in the reconstructed mass-mobility distribution based on the Mahalanobis distances between the points in $[\log_{10} d_\mathrm{m}, \log_{10} m]^\mathrm{T}$ space. The transfer functions in the kernel were evaluated using the analytical forms for diffusing flow given by Stolzenburg [29] for the DMA, Sipkens et al. [30] for the CPMA (specifically, Case 1C in that work), and the hybrid charging probabilities described in Ref. [28].

In this latter interpretation, which we denote as the *distribution-based approach*, the set of morphological parameters was derived by fitting a bivariate lognormal distribution (joint-normal in $[\log_{10} d_\mathrm{m}, \log_{10} m]^\mathrm{T}$ space) to the reconstructions. The bivariate lognormal distribution has the form [28],

$$\frac{\partial^2 n}{\partial \log_{10} m \cdot \partial \log_{10} d_\mathrm{m}} \propto \det(2\pi\boldsymbol{\Sigma})^{-1/2} \exp\left(-\frac{1}{2}(\mathbf{r}-\boldsymbol{\mu})^\mathrm{T}\boldsymbol{\Sigma}^{-1}(\mathbf{r}-\boldsymbol{\mu})\right), \tag{5}$$

where $\mathbf{r} = [\log_{10} m, \log10 d_\mathrm{m}]^\mathrm{T}$ is some point in logarithmic mass-mobility space; $\boldsymbol{\mu} = [\log_{10} m_\mathrm{g}, \log_{10} d_{\mathrm{m,g}}]$ is the mean of the distribution in logarithmic mass-mobility space, where m_g and $d_{\mathrm{m,g}}$ are the median (or geometric mean) mass and mobility of the particle population, respectively; and $\boldsymbol{\Sigma}$ is the mass-mobility covariance, which can be related to the distribution widths and the mass-mobility exponent, D_m, following

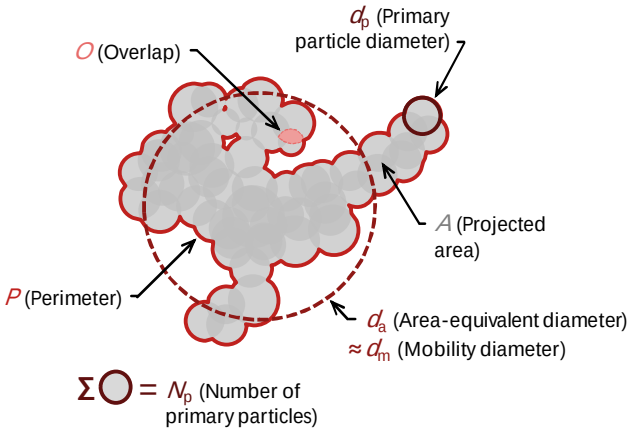

Figure 2. An illustration of the morphological parameters for aggregates, including the primary particle diameter, projected area diameter, and particle perimeter.

Sipkens et al. [28] and the supplemental material for this work. Briefly, $D_m = \Sigma_{1,2}/\Sigma_{2,2}$, $\sigma_m = 10^{\mathrm{sqrt}(\Sigma_{1,1})}$, and $\sigma_d = 10^{\mathrm{sqrt}(\Sigma_{2,2})}$. It is worth noting that this allows for an expanded set of morphological parameters that includes the population-level and conditional distribution widths.

In this latter representation, the inverted mass-mobility distributions can also be transformed to effective density-mobility distributions by a linear transformation, as described in the supplemental material. It is also shown that if the mass-mobility distribution is bivariate lognormal, the effective density-mobility distribution will also be bivariate lognormal.

2.2 Transmission electron microscopy analysis

Transmission electron microscopy (TEM) samples were collected on 3 mm carbon type-B copper TEM grids (Ted Pella, 01813, 300 mesh) using a thermophoretic sampler (TPS) developed at the University of British Columbia. Images were taken with a Hitachi H7600 TEM at an accelerating voltage of 80 kV. To simplify analysis and because quantities like the fractal dimension and number of primary particles are often poorly characterized by two-dimensional images [33, 34, 35, 36], we limit our consideration to the projected area-equivalent diameter, d_a, and primary particle diameter, d_p, which are sufficiently accurate for two-dimensional images [36]. Figure 2 illustrates the physical definition of these two parameters, among others.

The projected-area-equivalent diameter, d_a, and mean primary particle size, $\overline{d}_p$, of soot were analyzed using an automated image analysis code developed by Dastanpour, Boone and Rogak [37], which employs

the pair correlation method (PCM) to estimate $\bar{d}_p$ within each particle. It relies on the assumption that the primary particles within an aggregate are approximately uniform in size which has been observed for many soot sources [38]. In addition to reporting mean values from traditional lognormal fits, the $\bar{d}_p$ and d_a data extracted from the images were also fit to a power law of the form:

$$\bar{d}_p = \bar{d}_{p,100}\left(\frac{d_a}{100}\right)^{D_{TEM}} \quad (6)$$

where $\bar{d}_{p,100}$ is the average primary particle diameter of a particle with d_a = 100 nm, D_{TEM} is the power law exponent, and d_a is given in nm. The two parameters were fit with a linear regression in logarithmic space. From this fit it is possible to derive effective density as described by Olfert and Rogak [24]. Briefly, Eggersdorfer et al. [39] gives an equation which relates effective density to mobility diameter. First, the Sauter mean diameter of the primary particles, d_{va}, is assumed to be equivalent to the primary particle diameter derived from TEM ($d_{va} \sim \bar{d}_p$). The projected-area-equivalent diameter is assumed to be equivalent to the mobility diameter ($d_a \sim d_m$). This assumption is only strictly valid in the free molecular regime but extends well to the transition regime. In the continuum regime this assumption results in a ~10% error in estimated d_m [40, 41] which corresponds to a ~ 5% change in effective density and a ~ 3% change in estimated primary particle size. which allows for the calculation of the effective density of a particle given $\bar{d}_p$ and d_a,

$$\rho_{eff} = k_a \rho \left(\frac{\bar{d}_p}{d_a}\right)^{3-2D_\alpha} \quad (7)$$

where the material density of soot, ρ, is assumed to be 1800 kg/m^3 [42, 43]; D_α is the projected-area exponent; and k_a is the prefactor. Dastanpour et al. [44] optimized the latter parameters for soot and found D_α = 1.1 and k_a = 1.13, which additionally compensates for small errors due to the assumption $d_a \sim d_m$. These values were used to estimate the effective density of soot particles from gas flares with good agreement to measured values by Kazemimanesh et al. [23]. The results can be compared to the SMPS-CPMA results following a transformation of the mass-mobility distribution to effective density-mobility space.

2.3 Raman Spectroscopy

Samples for Raman spectroscopy were collected on titanium substrates with the same thermophoretic sampler used to collect the TEM samples. A Renishaw Confocal Raman spectrometer was used with a 785 nm laser point focus at an energy of 0.2 mW, with exposure and integration times set to 10 s and 1 s, respectively. OriginPro (version 2017) was used to deconvolute the Raman spectra with the five-bands method. Three independent spectra were measured and averaged for each sample. The five bands selected for Raman deconvolution were [45]: D4 (1127 cm^{-1} to 1208 cm^{-1}), D1 (1301 cm-1 to 1317 cm-1), D3 (1489 cm-1 to 1545 cm-1), G (1571 cm-1 to 1598 cm-1), D2 (1610 cm-1 to 1625 cm-1). A detailed description of the Raman analysis is provided by Baldelli and Rogak [47]. The stability of the procedure in Raman deconvolution was demonstrated in Popovicheva et al. [24]. In this study the ratio of the D peaks to the G peak is reported as a measure of the level of order or disorder within the nanostructure with larger values indicating a more disordered nanostructure.

3. Results and discussion

3.1 Primary particle size

Table 1
A summary of TEM results from select fuels. Median primary particle diameter and projected-area-equivalent diameter using a lognormal fit are compared to power law fits for the same data. Primary particle diameter from the power law fit at the median aggregate size is also listed.

Fuel Code	HHVv [MJ/m^3]	Median d_p	Median d_a	$d_{p,100}$ ± 95% CI	D_{TEM} ± 95% CI
L6*	35.3	-	-	16.5 ± 0.5	0.45 ± 0.04
L9	35.8	15.0	104	14.8 ± 1.0	0.34 ± 0.09
M9	41.6	16.4	122	15.0 ± 1.0	0.44 ± 0.07
H9	47.0	17.7	135	16.1 ± 0.8	0.28 ± 0.06
M6*	48.5	-	-	17.1 ± 0.9	0.54 ± 0.07
RU-KM1	51.4	17.6	134	16.5 ± 1.2	0.29 ± 0.09
EC-AC	54.6	20.6	174	16.7 ± 1.6	0.38 ± 0.09
H6*	54.7	-	-	17.9 ± 1.0	0.52 ± 0.07
BK-BR	61.1	21.5	147	18.9 ± 1.4	0.32 ± 0.09
EC-AC27	75.2	25.0	262	16.2 ± 2.0	0.40 ± 0.10
L9 + Water	35.8	16.3	97	16.5 ± 1.1	0.36 ± 0.08
M9 + Water	41.6	14.8	102	14.7 ± 0.7	0.31 ± 0.06
H9 + Water	47.0	16.0	131	14.7 ± 0.8	0.28 ± 0.06

* Fuels where data was adopted from the work of Kazemimanesh et al. [23]

TEM images were used to determine the average primary particle diameter, d_p, and projected-area-equivalent diameter, d_a, of each aggregate imaged. Traditionally, these data are fit to a lognormal distribution to extract the median values of d_p and d_a the results of which are summarized in Table 2. Additionally, power law relationships were fit to the data points. Figure 3a shows a scatter plot of each data point collected, the dashed lines shows the *universal fit* proposed by Olfert and Rogak [24] and the best fit for these data. Figure 3b shows the fits for each fuel based on the data from Figure 3a. The aggregates collected here are very similar to the universal fit and are statistically indistinguishable from one another when considering the overlap from the 95% confidence intervals. The median values show an increase in median primary particle diameter with HHVv; however, the aggregate diameter is also increasing with HHVv, approximately as suggested by the scaling relation given in Olfert and Rogak [24]. Similarly, the addition of water slightly reduces the median aggregate size which in turn slightly decreases the median primary particle size while $d_{p,100}$ remains almost the same. The universal fit from Olfert and Rogak [24] was fit using the same methods with data from compression ignition engines, low pressure burners, GDI engines and gas turbines and is very similar to the data presented here. The combined relationship found in this work,

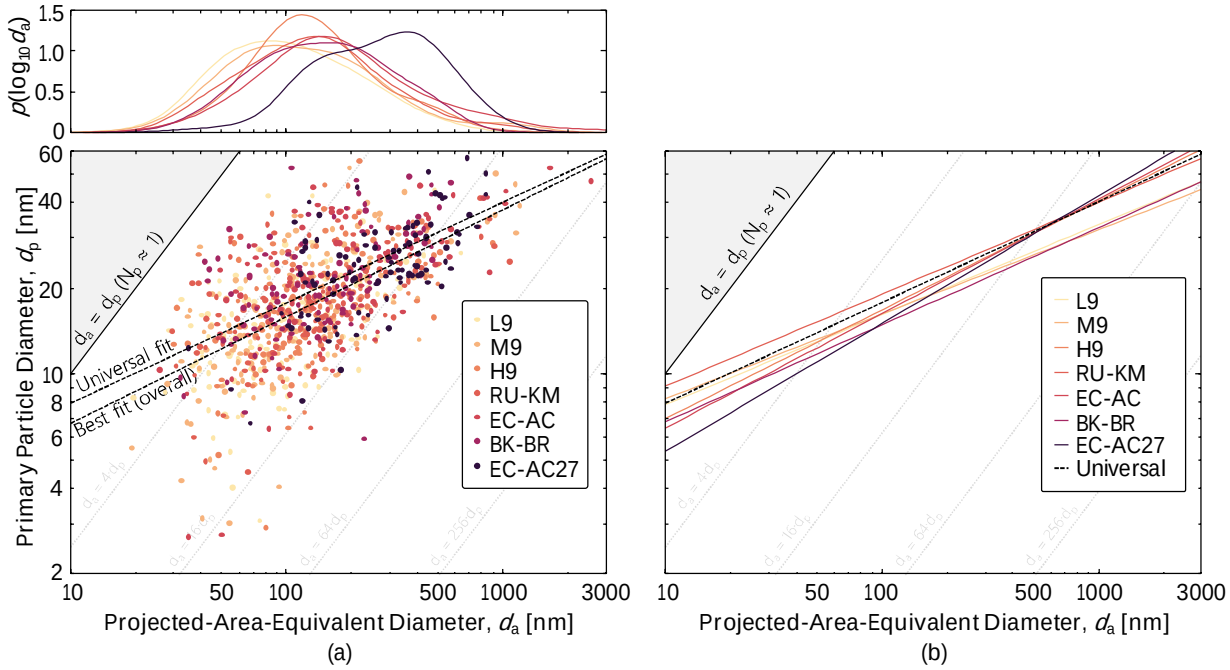

Figure 3. (*a*) Raw data and (*b*) power law fits to the relationship between primary particle diameter and projected-area-equivalent diameter derived from TEM data. The upper panel of (*a*) shows kernel density estimates of the distribution of the area-equivalent diameter, $p(\log_{10}d_a)$,with consistent colours to the other panels. Light grey lines, in both panels, indicate isolines of particles where d_a is a certain multiple of the d_p (e.g. $d_a = d_p$ corresponds to monospheres).

$$d_p = 16.3\left(\frac{d_a}{100}\right)^{0.35}, \tag{8}$$

is similar to that reported by Kazemimanesh et al. [23],

$$d_p = 17.7\left(\frac{d_a}{100}\right)^{0.44}, \tag{9}$$

where, in both cases, d_a is given in nm. Thus, we can conclude that the fuel has little to no effect on the relationship between d_p and d_a.

3.2 Mobility distribution

Figure 4 shows SMPS-derived mobility distributions for the available fuels. Fuels are colour-coded based on their HHVv while blue dashed lines denote cases with water addition. Arrows illustrate which 'dry' fuels have a corresponding water-added case. The median diameter and geometric standard deviation were derived from the scans using least-squares fits of a lognormal distribution to the SPMS scans, with the results reported in Table 2. The authors note that fits were slightly biased by a heavier lower tail than would be predicted if the SMPS distributions were truly lognormal. This biases the median diameter

towards smaller particle sizes and causes a larger distribution width. For fuels from L9 (HHVv = 35.8 MJ/m^3) to EC-AC (HHVv = 54.6 MJ/m^3), the number concentration and median soot diameter rise with increasing HHVv, indicating the expected trend towards higher soot yields for heavier fuels. These trends diminish for fuels with an HHVv above 55 MJ/m^3, where the sooting propensity appears to saturate. RU-FI (HHVv = 71.5 MJ/m^3) and RU-KM1 (HHVv = 51.4) are exceptions to this trend, with higher soot concentrations compared to fuels with similar HHVv. This is likely related to differences in fuel composition which are not easily summarized by the HHVv alone. The HHVv nonetheless predicts the soot quantity very well considering its simplicity.

3.3 Mass-mobility distribution

Two-dimensional mass-mobility distributions were derived from the tandem CPMA-SMPS measurements as described in Section 2.1 and Ref. [28]. A sample two-dimensional mass-mobility distribution for the M9 fuel is shown in Figure 5a, with the mass-mobility distributions for the other cases included in the supplemental material. Marginal distributions, integrating over each dimension to get distributions of the mobility and mass alone, are shown on either axis and reasonably resemble those resulting from the SMPS only analysis in Section 3.2. The distributions all exhibit the expected single mode and appear to be approximately bivariate lognormal. There exists a small amount of flaring in the

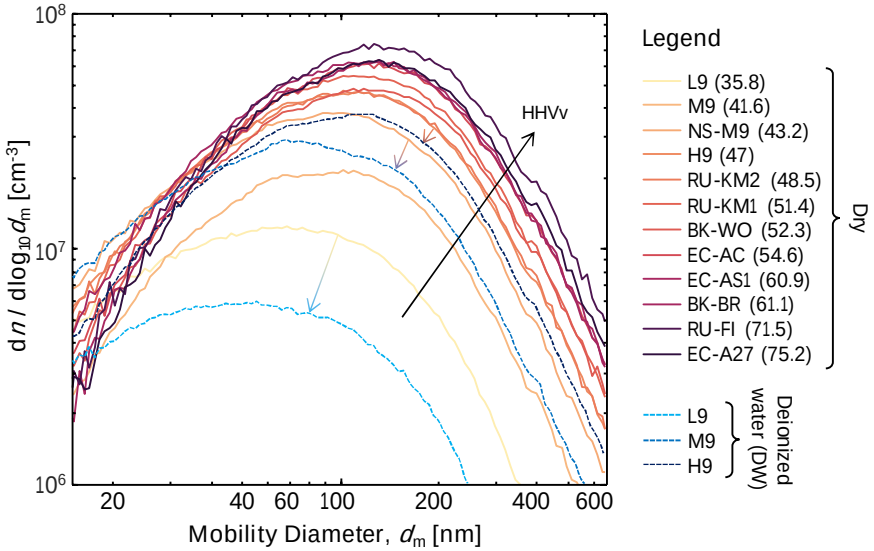

Figure 4. Distribution of the mobility diameter derived from SMPS measurements for all of the dry fuel cases. The line color scales with the HHVv of the fuels, indicated in brackets in the legend. Deionized water cases are shown with dashed, blue lines. Arrows denote which dry-fuel case corresponds to which water-added case.

Table 2
Relevant aggregate morphological parameters derived from the SMPS only and tandem SMPS-CPMA analysis. For the tandem measurements, both the results of the more traditional median-based and the newer distribution-based approach are indicated.

		SMPS only		Tandem, median-based approach			Tandem, distribution-based approach							
Fuel Code	HHVv [MJ/m^3]	$d_{m,g}$ [nm]	σ_{dm}	D_m	m_{100} [fg]	$\rho_{eff,100}$ [kg/m^3]	$d_{m,g}$ [nm]	σ_{dm}	m_g [fg]	σ_m	D_m	m_{100} [fg]	$\rho_{eff,100}$ [kg/m^3]	$\sigma_{m\|dm}$ [fg]
L9	35.8	129	2.36	2.61	0.307	587	116	1.69	0.461	3.65	2.40	0.320	612	1.37
M9	41.6	156	2.18	2.61	0.374	714	117	1.86	0.548	4.61	2.40	0.380	725	1.42
NS-M9	43.2	167	2.29	2.59	0.377	720	116	1.94	0.544	5.21	2.42	0.377	720	1.43
H9	47.0	179	2.22	2.65	0.343	655	151	1.73	0.968	3.86	2.36	0.367	702	1.48
RU-KM2	48.5	183	2.24	2.68	0.348	665	140	1.81	0.832	4.37	2.41	0.368	702	1.48
RU-KM1	51.4	190	2.19	2.65	0.350	668	148	1.82	0.938	4.36	2.38	0.369	706	1.49
BK-WO	52.3	197	2.17	2.62	0.362	691	145	1.84	0.917	4.47	2.38	0.376	718	1.47
EC-AC	54.6	199	2.13	2.64	0.370	707	145	1.89	0.932	4.80	2.37	0.388	741	1.49
EC-AS1[†]	60.9	199	2.10	-	-	-	-	-	-	-	-	-	-	-
BK-BR	61.1	199	2.18	2.62	0.354	676	163	1.81	1.196	4.29	2.35	0.382	729	1.52
RU-FI[†]	71.5	215	2.14	-	-	-	-	-	-	-	-	-	-	-
EC-AC27	75.2	207	2.12	2.53	0.397	758	156	1.87	1.163	4.49	2.32	0.415	793	1.48
Average	53.6	185	2.19	2.62	0.358	684	140	1.82	0.850	4.41	2.38	0.374	715	1.46
Std. dev.	11.3	23	0.07	0.04	0.024	46	17	0.08	0.256	0.44	0.03	0.024	45	0.04
Universal fit [25]	-	-	-	2.48	0.267	510	-	-	-	-	2.48	0.267	510	-

[†] Tandem measurements were not available for these fuels.

distributions, where the conditional distribution width increases slightly with increasing particle mass and mobility diameter. Fits of the mass-mobility relation, Eq. (1), to the tandem measurements were computed using both the median- and distribution-based approaches. The resultant curves are indicated in Figure 5b, along with the median implied by the mass-selected SMPS scans.

Table 2 indicates that the median-based analysis of the data yields values for D_m, m_{100}, and $\rho_{eff,100}$ that are relatively consistent across the fuels. This independence of fuel type suggests that the particle shape changes little with fuel, even as the median particle diameter increases. The values here lie systematically above those the universal fit, which was found to describe a wide range of soot sources [24]. While there was a consistent shift, the parameters of the universal fit still lie within 25% of the average over all of the fuel types. The authors note that weighting the median diameters during fitting considerably reduced the spread observed across the different fuels, improving the robustness of the analysis.

For the distribution-based approach, many of the inferred values remain independent of the fuel, again including the mass-mobility exponent and the properties of particles that share a mobility diameter of 100 nm, m_{100} and $\rho_{eff,100}$. It was notable that the spread in the inferred parameters across the fuels was approximately the same as the median-based approach without requiring any data weighting, a reflection of the fact that the distribution-based approach was less susceptible to biases in the tail regions of the distribution. This was reinforced by the observation in Figure 5b that the median-based approach contained a potential outlier (the median of the lowest mass SMPS scan, even if this point is weighted lightly) and that the weighting procedure appears to undervalue the medians of the higher mass SMPS scans. The latter has the consequence of producing larger mass-mobility exponents for the median-based analysis, while the distribution-based analysis resulted in mass-mobility exponents is closer to the universal relation [25]. Though the parameter was somewhat sensitive to the regularization parameter chosen in the inversion scheme. It is also notable that the m_{100} and $\rho_{eff,100}$ inferred with the distribution-based method are increasingly divergent from the universal relation, in part a consequence of the universal expression having been derived from prior median-based analyses. Proceeding, unlike m_{100} and $\rho_{eff,100}$, the median mobility

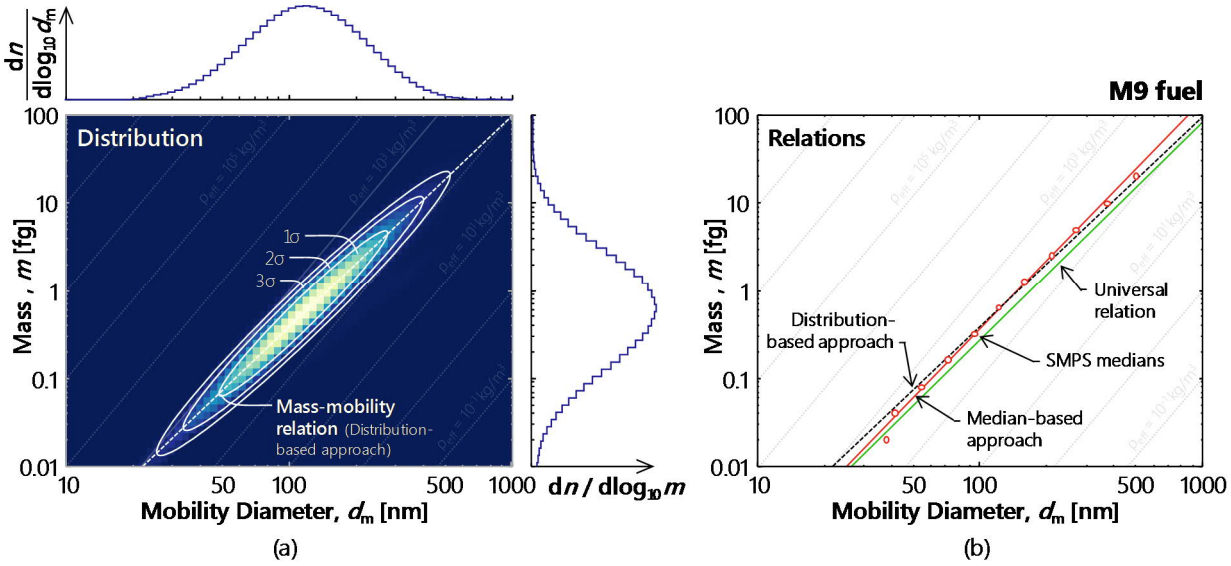

Figure 5. (*a*) Reconstructed mass-mobility distribution for the M9 fuel, where brightness indicate relative number of particles on a linear scale. Ellipses represent isolines corresponding to one, two, and three standard deviations away from the mean of a bivariate lognormal distribution fit to the data. Also indicated is the mass mobility relation implied by the distribution-based approach, with parameters indicated in Table 2. Normalized marginal distributions for each of the variables are shown on the corresponding axis, found by integrating the distribution in the corresponding direction. (*b*) Mass-mobility relations in $[\log_{10}m, \log_{10}d_m]^T$ space, including that given by the median- and distribution-based approaches and the universal relation from Olfert and Rogak [24]. Both panels share the same scales.

diameter and particle mass increase significantly with HHVv. This is consistent with the findings of the SMPS-only analysis and indicates that the heavier fuels generally have a higher sooting propensity. When combined with observations of the relative invariance of the properties of particles that share a mobility diameter of 100 nm, these observations are consistent with the theory that the higher HHVv fuels produce larger particles that maintain a similar shape. This is further affirmed in that the width of the conditional mobility and mass distributions are also consistent across the fuels affirming a shift in the overall size of the particles rather than other morphological changes.

Conditional mobility distribution widths retrieved from the distribution-based analysis tended to be narrower than the SMPS-only analysis. This was partially a consequence of structure in the error between the lognormal fits and the SMPS scans, which tended to give slightly wider distributions and larger median diameters. This may also stem from limitations in the default inversion performed on-board the SMPS.

3.4 Effective Density

Effective density is calculated in three ways: using both the median- and distribution-based analyses of the CPMA-SMPS measurements and using the TEM data with Eq. (7) [24]. In this way, the quantity acts to bridge between the population-level statistics provided by the CPMA-SMPS measurements and the limited number of aggregates analyzed using TEM. The results of all three methods are shown in Figure 6, where (a) gives an indication of the distribution of the quantities and (b) gives the series of relations derived from the data as well as the universal expression of Olfert and Rogak [24].

While the two-dimensional CPMA-SMPS and TEM distributions had similar widths and slopes (i.e. similar mass-mobility exponent) and overlapped significantly, there is some discrepancy in the distribution means derived from the two sets of data where the CPMA-SMPS distributions are shifted to larger masses. These discrepancies, although visually noticeable, still fall within the expected ± 20% variation for this type of measurement [24]. Effective density measurements reported by Kazemimanesh et al. [23] also fall within this range.

3.5 Raman analysis

Raman D1/G ratios are plotted as a function of a fuel's volumetric higher heating value in Figure 7. Fuels which are described in this study are denoted with open circles, those from Kazemimanesh et al. [23] are denoted with solid circles. Fuel HHVv is denoted with the same colour-code used previously and square, blue symbols indicate cases with water added. Error bars represent the standard deviation of results from three spectra from the same sample. For all four ratios, there is a clear trend of increasing graphitization, or decreasing disorder, as HHVv increases. Square symbols denote L9, M9 and H9 fuels with the addition of water. For each fuel the addition of water has no discernible effect on the results. Similar trends were seen for the D2/G, D3/G and D4/G ratios which can be found in the supplemental information.

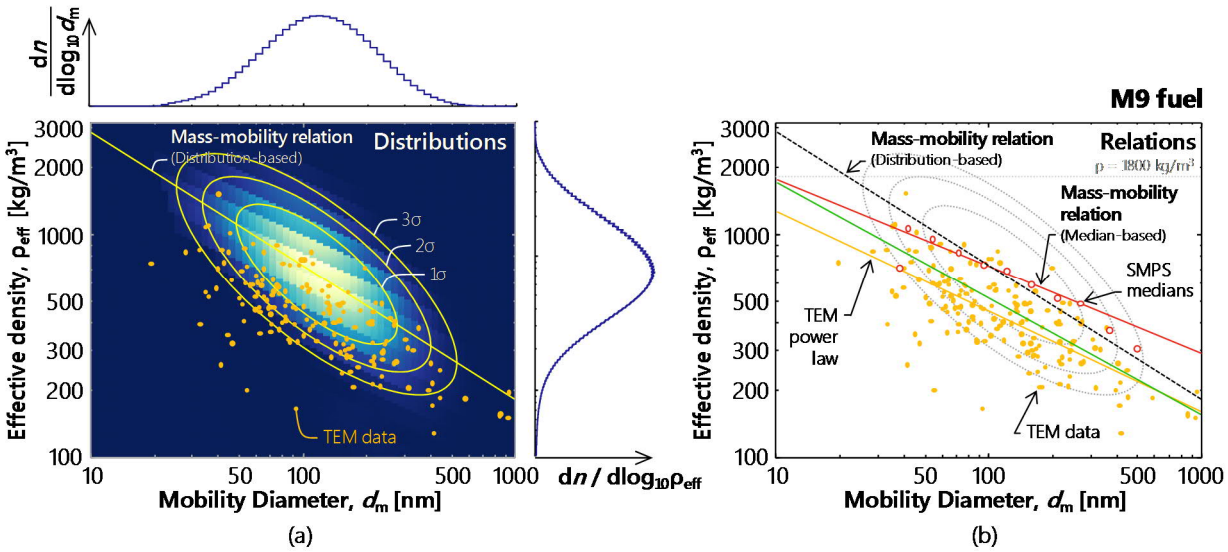

Figure 6: (*a*) Two-dimensional representation of the effective density-mobility distribution, where brightness indicate relative number of particles on a linear scale, from the CPMA-SMPS measurements and TEM data for the M9 fuel. (*b*) The corresponding relations derived using a series of methods, including effective densities derived from the mass-mobility relations in Figure 5b, the TEM-based power law from Figure 3, and the universal fit from Olfert and Rogak [24].

Studying the soot produced by a small laminar ethylene flame and collected on different impactor stages, Baldelli and Rogak [47] observed that larger aggregates, which tend to have larger primary particles, also have lower D/G ratios. Specifically, the D1/G ratio decreased from 13 to 9 as d_p increased from 16 to 25 nm. For the flare soot, the D1/G ratio decreases from 11 to 5 as median primary particle increases from 15 to 25 nm (this increase was associated with larger HHVv, Table 2). It is possible the size of the primary particle influences the Raman spectra, but it is more likely that the flame residence time and fuel composition result in slightly different trends.

4. Conclusions

Fuel composition results in significant differences in soot aggregate size and number concentration, with little effect on the structure of the aggregates. Fuels with a greater HHVv produce, on average, larger aggregates in greater quantities than fuels with a lower HHVv. This corresponds to an increase in primary particle size, consistent with previous findings [38]. If the primary particle size for a single aggregate size ($d_{p,100}$ for aggregates 100 nm in diameter) is considered, then the average primary particle sizes for all of the fuel cases is the same to within a few nanometers.

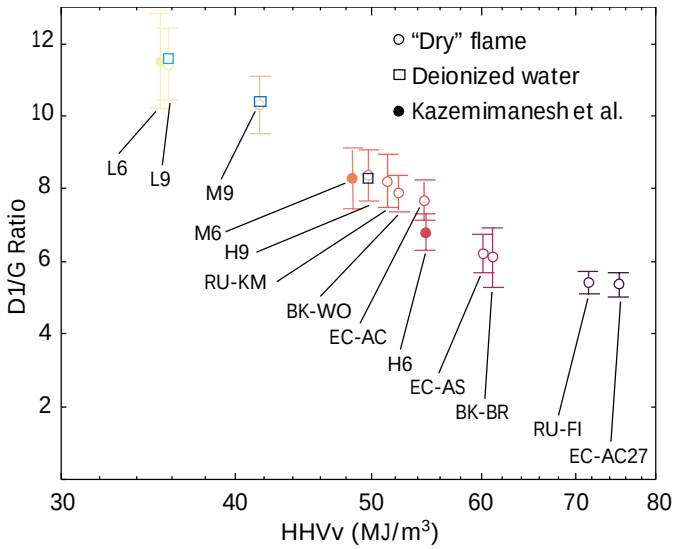

Figure 7. D1/G ratios of Raman samples as a function of the fuel's volumetric higher heating value. Fuels which are considered in this study are denoted with open circles. Solid circles denote results from the study by Kazemimanesh et al. **[23]**. D1/G ratios for cases with water addition are shown with blue squares. Error bars associated with the deionized water are nearly identical to the error bars of the associated dry case.

The D/G ratios for fuels with greater HHVv become smaller indicating an increasingly graphitic structure. This change is associated with an increase in the average primary particle size, roughly consistent with previous observations for size-segregated soot from a small ethylene burner. Water addition to the flame reduced soot yields but had no significant effect on the Raman spectra or the value of d_{p100}.

The particle effective density is determined through multiple complimentary methods, including inversion to find a two-dimensional mass-mobility distribution from tandem CPMA-SMPS scans and an estimation from TEM. In all cases, the effective density of the particles tends to be consistent across the full range of fuels. Two-dimensional representations of the tandem CPMA-SMPS data tended to be more consistent than the traditional representations in that D_m is closely clustered about the mean across the fuels, without requiring data weighting.

5. Data availability

The data has been made available in the supplemental material.

Acknowledgements

This work was funded by the Natural Science and Engineering Research Council of Canada (PDF-516743-2018; FlareNet Strategic Network, 479641) and the Canadian Council for the Arts (Killam Postdoctoral Fellowship).

6. References

[1] C. D. Elvidge, M. Zhizhin, K. Baugh, F.-C. Hsu and T. Ghosh, "Methods for Global Survey of Natural Gas Flaring from Visible Infrared Imaging Radiometer Suite Data," Energies, vol. 9, no. 1, p. 14, 2016.

[2] C. Murphy-McGreevey, "Increased Shale Oil Production and Political Conflict Contribute to Increase in Global Gas *Flaring*," World Bank, 16 06 2019. [Online]. Available: http://www.worldbank.org/en/programs/gasflaringreduction. [Accessed 23 09 2019].

[3] T. J. Luben, J. L. Nichols, S. J. Dutton, E. Kirrane, E. O. Owens, L. Datko-Williams, M. Madden *and J. D.* Sacks, "A systematic review of cardiovascular emergency department visits, hospital admissions and mortality associated with ambient black carbon," *Environ. Int.*, vol. 107, pp. 154-162, 2017.

[4] M. C. Power, M. G. Weisskopf, S. E. Alexeeff, B. A. Coull, A. Spiro III and J. Schwartz, "Traffic-related air pollution and cognitive function in a cohort of older men," *Environ. Health Perspect.*, vol. 119, no. 5, pp. 682-687, 2010.

[5] D. Maynard, B. A. Coull, A. Gryparis and J. Schwartz, "Mortality risk associated with short-term exposure to traffic particles

and sulfates," Environ. Health Perspect., vol. 115, no. 5, pp. 751-755, 2007.

[6] T. C. Bond, S. J. Doherty, D. W. Fahey, P. M. Forster, T. Berntsen, B. J. DeAngelo, M. G. Flanner, S. Ghan, B. Kärcher, D. Koch and S. Kinne, "Bounding the role of black carbon in the climate system*: A scientific assessment,"*J. *Geophys. Res. D: Atmos.,* vol. 118, no. 11, pp. 5380-5552, 2013.

[7] J. H. Scheckman and P. H. McMurry, "Deposition of silica agglomerates in a cast of human lung airways: Enhancement relative to spheres of equal mobility and aerodynamic diameter," Journal of Aerosol *Science,* vol. 42, pp. 508-516, 2011.

[8] K. Carslaw, L. Lee, C. Reddington, K. Pringle, A. Rap, P. Forster, G. Mann, D. Spracklen, M. Woodhouse, L. Regayre and J. Pierce, "Large contribution of natural aerosols to uncertainty in indirect forcing," Nature, vol. *503, no.* 7474, pp. 67-71, 2013.

[9] IPCC, "Mitigation Pathways Compatible with 1.5C in the Context of Sustainable Development," Global Warming of 1.5C. An IPCC *Special Report on the impacts* of global warming of 1.5C above pre-industrial levels and related global *greenhouse gas emission pathways,* in the context of strengthening the global *response to the threat of climate change.,* p. In Press, 2018.

[10] M. G. Flanner, "Arctic climate sensitivity to local black carbon," Journal of Geophyiscal Research: Atmospheres, vol. 118, pp. 1840-1851, 2013.

[11] K. Law and A. Stohl, "Arctic air pollution: Origins and impacts," Science, vol. 315, no. 5818, pp. 1537-1540, 2007.

[12] A. Stohl, Z. Klimont, S. Eckhardt, K. Kupianinen, V. Shevchenko, V. Kopeikin and A. Novigatsky, "Black carbon in *the* Arctic: the underestimated role of gas flaring and residential combustion emissions," *Atmospheric Chemistry and Physics,* vol. 13, pp. 8833-8855, 2013.

[13] O. G. Fawolea, X.-M. Caia and A. MacKenzie, "Gas flaring and resultant air pollution: A review focusing *on black carbon,* *Environmental* Pollution, vol. 216, pp. 182-197, 2016.

[14] A. Roiger, J. L. Thomas, H. Schlager, K. Law, J. Kim, A. Schäfler, B. Weinzierl, *F. Dahlkötter,* I. Risch, L. Marelle, A. Minikin, J. C. Raut, A. Reiter, M. Rose, M. Scheibe, P. Stock, R. Baumann, I. Bouarar, C. C. Lerbaux, M. George, T. Onishi and J. Flemming, "Quantifying emerging local anthropogenic emissions in the arctic region: The access aircraft campaign experiment," *Bulletin of the American Meteorological Society,* vol. 96, no. 3, pp. 441-460, 2015.

[15] A. Gvakharia, E. A. Kort, A. Brandt, J. Peischl, T. B. Ryerson, J. P. Schwarz, M. L. Smith and C. Sweeney, "Methane, Black *Carbon,* and Ethane *Emissions from Natural Gas* Flares in the Bakken Shale, North Dakota," *Environmental Science and Technology,* vol. 51, pp. 5317-5325, 2017.

[16] C. L. Weyant, P. B. Shepson, R. Subramanian, C. M. O. L, A. Heimburger, D. McCabe, E. Baum, B. H. Stirm and T. *C. Bond,* "Black Carbon Emissions from Associated Natural Gas Flaring," Environmental Science and Technology, vol. 50, *no. 4, pp.* 2075-2081, 2016.

[17] J. P. Schwarz, J. S. Holloway, J. M. Katich, S. McKeen, E. A. Kort, *M. L. Smith, T. B.* Ryerson, C. Sweeney and J. Peischl, "Black Carbon Emissions from the Bakken Oil and Gas Development Region," *Environmental Science and Technology,* vol. 2, no. 10, pp. 281-285, 2015.

[18] E. C. Fortner, W. A. Brooks, T. B. Onasch, M. R. Canagartna, P. Massoli, J. T. Jayne, J. P. Franklin, W. B. Knighton, J. Wormhoudt, D. R. Worsnop, C. E. Kolb and S. C. Herndon, "Particulate Emissions Measured During the TCEQ Comprehensive Flare Emission Study," *Industrial and Engineering Chemisty Research,* vol. 51, pp. 12586-12593, 2012.

[19] B. M. Conrad and M. R. Johnson, "Field Measurements of Black Carbon Yields from Gas Flaring," Environmental Science and Technology, vol. 51, no. 3, pp. 1893-1900, 2017.

[20] M. R. Johnson, R. W. Devillers and K. A. Thomson, "A Generalized Sky-LOSA Method to Quantify Soot/Black Carbon Emission Rates in Atmospheric Plumes of Gas Flares," *Aerosol Science* and Technology, vol. 47, no. 9, pp. 1017-1029, 2013.

[21] M. R. Johnson, R. W. Devillers and K. A. Thomson, "Quantitative Field Measurement of Soot Emission from a Large Gas Flare *Using Sky-LOSA,"Environmental Science* and Technology, vol. 45, no. 1, pp. 345-350, 2011.

[22] B. M. Crosland, K. A. Thomson and M. R. Johnson, "Simultaneous instantaneous measurements of soot volume fraction, primary particle diameter, and aggregate size in turbulent buoyant diffusion flames," Proceedings of the Combustion Institute, vol. 35, pp. 1851-1859, 2015.

[23] M. Kazemimanesh, R. Dastanpour, A. Baldelli, A. Moallemi, K. A. Thomson, M. A. Jefferson, M. R. Johnson, S. N. Rogak and J. S. Olfert, "Size, effective density, morphology and nano-structure of soot particles generated from buoyant turbulent diffusion flames," *J. Aerosol Sci.,* vol. 132, pp. 22-31, 2019.

[24] O. Popovicheva, M. Timofeev, N. Persiantseva, M. A. Jefferson, M. Johnson, S. N. Rogak and A. Baldelli, "Microstructure and chemical composition of particles from small-scale gas flaring," *Aerosol Air Qual. Res.,* vol. 19, no. 10, pp. 2205-2221, 2019.

[25] M. R. Johnson and A. R. Coderre, "Compositions and greenhouse gas emissions factors of flared and vented gas in the Western Canadian Sedimentary Basin," Journal of the Air *and Waste Management* Association, vol. 62, no. 9, pp. 992-1002, 2012.

[26] J. Olfert and S. Rogak, "Universal relations between soot effective density and primary particle size for common combustion sources," Aerosol Sci. Technol., vol. 53, no. 5, pp. *485-492, 2019.*

[27] V. K. Rawat, D. T. Buckley, S. Kimoto, M. H. Lee, N. Fukushima and C. J. Hogan Jr, "Two dimensional size–mass *distribution function inversion from differential* mobility analyzer–aerosol particle mass analyzer (DMA–APM) measurements," J. *Aerosol Sci.,* vol. 92, pp. 70-82, 2016.

[28] D. T. Buckley, S. Kimoto, M. H. Lee, N. Fukushima and C. J. Hogan Jr, "Technical note: A corrected two dimensional data inversion routine for *tandem mobility-mass measurements*," J. Aerosol Sci., vol. 114, pp. 157-168, 2017.

[29] T. A. Sipkens, J. S. Olfert and S. N. Rogak, "Inversion methods to determine two-dimensional aerosol mass-mobility distributions: A critical comparison of established methods," J. Aerosol *Sci.,* vol. 140, p. 105484, 2020.

[30] T. A. Sipkens, J. S. Olfert and S. N. Rogak, "Inversion methods to determine two-dimensional aerosol mass-mobility distributions: Existing and novel Bayesian methods," Under preperation.

[31] M. R. Stolzenburg, "A review of transfer theory and characterization of measured performance for differential mobility analyzers," Aerosol Sci. Technol., vol. 52, *no. 10, pp.* 1194-1218, 2018.

[32] T. A. Sipkens, J. S. Olfert and S. N. Rogak, "New approaches to calculate the transfer function of particle mass analyzers," *Aerosol* Sci. Technol., vol. 54, no. 1, pp. 111-127, 2020.

[33] L. H. van Poppel, H. Friedrich, J. Spinsby, S. H. Chung, J. H. Seinfeld and P. R. Buseck, "Electron tomography of nanoparticle clusters: Implications for atmospheric *lifetimes and radiative* forcing of soot," Geophysical Research Letters , vol. 32, no. 24, pp. 1-4, 2005.

[34] G. Okyay, E. Héripré, T. Reiss, P. Haghi-Ashtiani, T. Auger and F. Enguehard, "Soot aggregate complex morphology: 3D geometry reconstruction by SEM tomography applied on soot issued from propane combustion," Journal of Aerosol Science, Vols. 63-79, p. 93, 2016.

[35] O. Orhan, E. Haffner-Staton, A. La Rocca and F. Michael, "Characterisation of flame-generated soot and soot-in-oil using electron tomography volume reconstructions and comparison with traditional 2D-TEM measurements," Tribology International*, vol. 104,* pp. 272-284, 2016.

[36] K. Adachi, S. H. Chung, H. Friedrich and P. R. Buseck, "Fractal parameters of individual soot particles determined using electron tomography: Implications for optical properties*,"Journal* of Geophysical Research Atmospheres, vol. 112, p. D14202, 2007.

[37] A. Baldelli, U. Trivanovic and S. Rogak, "Electron tomography of soot for validation of 2D image processing and observation of new structural features,"Aerosol Science & Technology, vol. 53, no. 5, pp. 575-582, 2019.

[38] R. Dastanpour, J. M. Boone and S. N. Rogak, "Automated primary particle sizing of nanoparticle aggregates by TEM image analysis," Powder *Technol.*, vol. 295, pp. 218-224, 2016.

[39] R. Dastanpour and S. N. Rogak, "Observations of a correlation between primary particle and aggregate size for soot particles," Aerosol Sci. Technol., vol. 48, no. 10, pp. 1043-1049, 2014.

[40] M. L. Eggersdorfer, A. J. Gröhn, C. M. Sorensen, P. H. McMurry and S. E. Pratsinis, "Mass-mobility characterization *of* flame-made ZrO2 aerosols: Primary particle diameter and extent of aggregation," *J. Colloid Interface Sci.,* vol. 387, no. 1, pp. 12-23, 2012.

[41] T. Thajudeen, S. Jeon and C. J. Hogan, "The mobilities of flame synthesized aggregates/agglomerates in the transition regime," Journal of *Aerosol* Science, vol. 80, *pp.* 45-57, 2015.

[42] S. N. Rogak, R. C. Flagan and H. V. Nguyen, "The Mobility and Structure of Aerosol Agglomerates," Aerosol Science and *Technology,* vol. 18, no. 1, pp. 25-47, 1993.

[43] T. C. Bond and B. R.W., "Light Absorption by Carbonaceous Particles: An Investivative Review," Aerosol Science and

Technology, vol. *40,* no. 1, pp. 27-67, 2006.

[44] F.-X. Ouf, S. Bourrous, S. Fauvel, K. A., L. Lintis, J. Nuvoli and J. Yon, "True density *of* combustion emitted particles: A comparison of results *highlighting the influence of* the organic contents," Journal of Aerosol Science, vol. 134, pp. 1-13, 2019.

[45] R. Dastanpour, S. N. Rogak, B. Graves, J. Olfert, M. L. Eggersdorfer and A. M. Boies, "Improved sizing *of* soot primary particles using mass-mobility measurements,"Aerosol Sci. Technol., vol. 50, no. 2, pp. 101-109, 2016.

[46] A. Sadezky, H. Muckenhuber, H. Grothe, R. Niessner and U. Pöschl, "Raman microspectroscopy of soot and related carbonaceous materials: spectral *analysis* and structural information," *Carbon,* vol. 43, no. 8, pp. 1731-1742, 2005.

[47] A. R. Baldelli and S. N. Rogak, "Morphology and raman spectra of aerodynamically classified soot samples," Atmos. Meas. Tech. Discuss., vol. 12, pp. 4339-4356, 2019.

[48] C. Sorenson, "Light Scattering by Fractal Aggregates: A Review," Aerosol Science & Technology, vol. 35, no. 2, pp. 648-687, 2001.